

Enhanced Magnetization by Defect-Assisted Exciton Recombination in Atomically Thin CrCl₃

Xin-Yue Zhang,^{1,*} Thomas K. M. Graham,^{1,*} Hyeonhu Bae,^{2,*} Yu-Xuan Wang,¹ Nazar Deegan,^{3,4,5} Jonghoon Ahn,^{3,4} Zhi-Cheng Wang,¹ Jakub Regner,⁶ Kenji Watanabe,⁷ Takashi Taniguchi,⁸ Minkyung Jung,⁹ Zdeněk Sofer,⁶ Fazel Tafti,¹ David D. Awschalom,^{3,4,5} F. Joseph Heremans,^{3,4,5} Binghai Yan,² and Brian B. Zhou^{1,†}

¹*Department of Physics, Boston College, Chestnut Hill, MA, 02467, USA*

²*Department of Condensed Matter Physics, Weizmann Institute of Science, Rehovot, Israel*

³*Materials Science Division, Argonne National Laboratory, Lemont, IL, 60439, USA*

⁴*Center for Molecular Engineering, Argonne National Laboratory, Lemont, IL, 60439, USA*

⁵*Pritzker School of Molecular Engineering, University of Chicago, Chicago, IL 60637, USA*

⁶*Department of Inorganic Chemistry, University of Chemistry and Technology Prague, Technicka 5, 166 28, Prague 6, Czech Republic*

⁷*Research Center for Electronic and Optical Materials, National Institute for Materials Science, 1-1 Namiki, Tsukuba 305-0044, Japan*

⁸*Research Center for Materials Nanoarchitectonics, National Institute for Materials Science, 1-1 Namiki, Tsukuba 305-0044, Japan*

⁹*DGIST Research Institute, DGIST, Daegu 42988, Republic of Korea*

(Dated: August 27, 2024)

Two dimensional (2D) semiconductors present unique opportunities to intertwine optical and magnetic functionalities and to tune these performances through defects and dopants. Here, we integrate exciton pumping into a quantum sensing protocol on nitrogen-vacancy centers in diamond to image the optically-induced transient stray fields in few-layer, antiferromagnetic CrCl₃. We discover that exciton recombination enhances the in-plane magnetization of the CrCl₃ layers, with a predominant effect in the surface monolayers. Concomitantly, time-resolved photoluminescence measurements reveal that nonradiative exciton recombination intensifies in atomically thin CrCl₃ with tightly localized, nearly dipole-forbidden excitons and amplified surface-to-volume ratio. Supported by experiments under controlled surface exposure and density functional theory calculations, we interpret the magnetically enhanced state to result from a defect-assisted Auger recombination that optically activates electron transfer between water vapor related surface impurities and the spin-polarized conduction band. Our work validates defect engineering as a route to enhance intrinsic magnetism in single magnetic layers and opens a novel experimental platform for studying optically-induced, transient magnetism in condensed matter systems.

Magnetic order in 2D semiconductors can modulate their reflection [1, 2] or absorption [3, 4] of polarized light, as well as the polarization [5, 6] or spectrum [7] of their photoluminescence (PL). These magneto-optical effects, which allow sensitive optical probing of the underlying magnetization, often hinge on the special properties of bound electron-hole pairs, known as excitons, that exhibit the enhanced Coulomb interactions [8, 9], spin-valley coupling [10], or interlayer hybridization [7] of the 2D limit. An intriguing prospect is whether the inverse effect occurs: can excitonic processes in a 2D semiconductor modify its magnetic properties? Such optical control of magnetism could enable low-power, high-speed spintronic devices featuring the versatility of the 2D materials platform [11–18].

In 2D magnets, such as the chromium trihalides (CrX₃, X = Cl, Br, I) [8, 9], transition metal dihalides MX₂ (X = Cl, Br, I) [19, 20], and transition metal phosphorus trichalcogenides MPX₃ (X = S, Se) [21–24], bonding between the transition metal and ligand atoms exhibits more ionic character than in the transition metal

dichalcogenides (TMDs). Ligand field theory thus serves as a starting point for understanding the optical excitations of 2D magnets, although considerations from band theory become necessary as the covalency of bonding increases [8, 9, 25]. In 2D magnets, excitons, appearing as sharp sub-bandgap peaks in the optical absorption, can be traced to the localized *d-d* transitions on the transition metal ions. Although parity-forbidden optically in the isolated atomic limit, these transitions become weakly allowed in crystals due to metal-ligand (*dp*) hybridization, as well as due to further symmetry breaking caused by the spin-orbit interaction or coupling to phonons and defects [25]. Consequently, these excitons can possess near-atomic spatial confinement and strong binding energies [26, 27] characteristic of Frenkel excitons in ionic insulators [28] or molecular crystals [29], exceeding that of Wannier-Mott excitons in the TMDs [30].

The strongly-correlated nature of excitons plays a vital role in imprinting the magnetic state of 2D semiconductors onto their optical response, for example through giant Kerr and Faraday effects [1, 8], spin-dependent absorption [3, 4] and photoluminescence [5–7], or ultra-narrow exciton linewidths stabilized by spin-orbit coherence [21, 31]. Alternatively, from the point of view of op-

* These authors contributed equally to this work.

† brian.zhou@bc.edu

tical control, ultrafast pump-probe measurements have demonstrated that $d-d$ excitons can generate magnons in bulk samples of NiPS₃ [23, 24], while circularly polarized ultrafast pulses at the charge-transfer exciton energy were shown to switch the magnetic state of three-layer CrI₃ [12]. Nevertheless, the distinct interactions of these strongly-bound excitons with defects and interfaces, and the novel routes by which they can modulate magnetism, particularly in atomically-thin samples, have yet to be fully elucidated.

In this work, we introduce pump-probe nitrogen-vacancy (NV) center magnetometry for the spatiotemporal imaging of optically controlled magnetism. By pumping the excitonic resonances in few-layer, antiferromagnetic (AF) CrCl₃, we discover that its in-plane, layer-alternating magnetization is remarkably increased within the pump spot by up to $0.5 \mu_B/\text{nm}^2$ in odd-layer regions, where μ_B is the Bohr magneton. The transient stray field due to this optical enhancement provides sensitive even-odd layer contrast as a local signature in the flake's interior, in distinction to the static stray field that diminishes away from the edges.

We correlate the formation of the magnetically enhanced state with a defect-assisted Auger recombination [32, 33] that predominates for excitons in CrCl₃, the most Frenkel-like within the CrX₃ family [25]. Time-resolved PL measurements probing the dynamics of exciton recombination reveal that this nonradiative pathway intensifies in thinner, unencapsulated flakes, confirming the role of surface impurities. Crucially, regions with higher rates of nonradiative exciton recombination display stronger optically-induced magnetization. The latter persists for tens of microseconds, exceeding the exciton lifetime and reflecting the slow charge trapping dynamics after recombination. Through measurements on a CrCl₃ flake sequentially exposed to water vapor (H₂O) and oxygen gas (O₂), we demonstrate control over the amplitude of the transient magnetization and pinpoint H₂O exposure as the primary catalyst. Our density functional theory (DFT) calculations support that H₂O adsorbates can introduce midgap states that mediate Auger recombination of excitons. This process could enhance the magnetization of CrCl₃ by transferring unpolarized defect electrons into the majority spin conduction band of its host surface layer.

Our results provide a demonstration of defect-modulation of the magnetic properties of single atomic layers with intrinsic order. Although proposed in numerous computational studies [34–39], this tuning knob, with strategies unique to the 2D limit such as molecular adsorption demonstrated here, has eluded experimental realization due to stringent requirements on control samples and quantitative magnetic measurement. Our light-activated charge transfer is distinct from other mechanisms for optical control of magnetism, such as through the absorption-induced occupation of a short-lived excited state with different magnetic exchange [40, 41] or through nonlinear field-induced effects, such as the in-

verse Faraday effect or inverse Cotton-Mouton effects, that require high intensity and suitably polarized light [42]. Charge transfer effects have been observed in ensembles of molecular magnets [43] and semiconductor quantum dots [44], but are revealed here for an atomically thin antiferromagnet through a pioneering, spatially-resolved technique. Thus, our discovery opens a high-speed, high spatial resolution avenue to control the doping and magnetic properties of atomically-thin magnets using light.

A. In-Plane, AF Interlayer Order

Below its Néel temperature $T_N \approx 17$ K, bulk CrCl₃ possesses moments that order ferromagnetically in-plane within each layer, but antiferromagnetically between adjacent layers [45]. As in-plane magnetization cannot be detected via magneto-optical effects using light at normal incidence, magnetic order in atomically-thin CrCl₃ has only been investigated by tunneling magnetoresistance [46–49] and x-ray magnetic circular dichroism at grazing incidence [50], which both possess limited spatial resolution. To overcome this lack of spatial information, we leverage magnetic imaging by NV spins in diamond, previously employed to visualize the out-of-plane magnetic order in CrI₃ and CrBr₃ [51–53]. In extension to prior works, here we implement a geometry optimized for high-sensitivity ac magnetometry [54] and pump-probe optical access [55]. Few-layer CrCl₃ flakes, encapsulated by hBN unless otherwise described, are transferred inside an argon-filled glovebox onto a ¹²C isotopically-enriched diamond substrate containing a near-surface NV ensemble with prolonged coherence time (Appendix A). As illustrated in Figs. 1a,b, the pump beam of variable wavelength (405–785 nm; shown in red) excites exciton dynamics in CrCl₃, while an independently steered probe beam (green, 515 nm) images the resulting stray magnetic field across the NV ensemble at diffraction-limited spatial resolution.

We begin by performing pulsed optically detected magnetic resonance (ODMR) to determine the static, layer-dependent magnetization in CrCl₃ flakes at $T = 4$ K. In this mode, the NV spin transitions are Zeeman-shifted by the dc stray field along the NV center axis, angled at $\theta = 35^\circ$ from the surface in the xz -plane (Fig. 1a) [51]. We apply a bias field B_{ext} along the NV center axis and define the quantity B_{NV} to be solely the field due to the flake by subtracting B_{ext} from the measured total field.

Figure 1c shows the image of B_{NV} at small $B_{ext} = 3.3$ mT for the CrCl₃ flake depicted in Fig. 1a, containing regions with four to nine layers. Significant stray fields are detected over the odd-layer regions, in contrast to negligible stray fields over the even-layer regions, except over a narrow 6/8-layer stripe where the signal is contributed by its two neighboring odd layers. In Fig. 1d, we simulate the flake's stray field assuming AF interlayer magnetic order oriented along the in-plane projec-

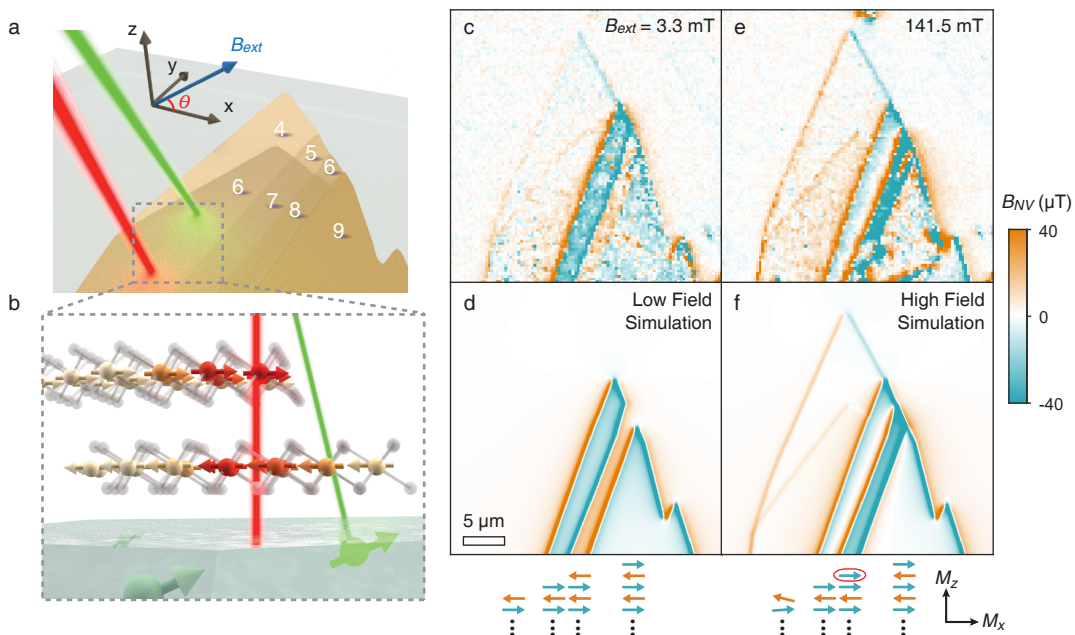


FIG. 1. Experimental background. (a) Few-layer CrCl_3 flakes are transferred onto a diamond substrate (gray) containing a near-surface ensemble of NV centers. NV magnetic imaging is performed by scanning the green probe beam (515 nm), while exciton dynamics in CrCl_3 are stimulated by the “red” pump beam (variable wavelength). (b) The layer magnetization in CrCl_3 lies in-plane and alternates antiferromagnetically between layers, producing a stray magnetic field sensed by proximal NV centers (green). (c) Experimental dc stray field (B_{NV}) image of a CrCl_3 flake, with 4 to 9-layer regions as labeled in panel a), at low external field B_{ext} . (d) Simulation of B_{NV} assuming in-plane, AF interlayer order. The bottom cartoon displays the magnetization of the top-most layers for the vertically adjacent region, showing odd-layer regions to possess an uncompensated monolayer along the in-plane projection of B_{ext} . (e) Experimental B_{NV} image at high B_{ext} . (f) Simulation of B_{NV} assuming that one layer of spins (circled) within the 6/8-layer stripe flips, resulting in two uncompensated layers.

tion of B_{ext} ($+\hat{x}$) [56]. This simulation reproduces the salient even-odd stray field contrast, as well as the detailed spatial parity of the stray field, which is inconsistent with out-of-plane magnetic order (Supplementary Fig. 1). Quantitative linecuts presented in Supplementary Fig. 1e reveal that the areal magnetization of the 5/7-layer stripe is approximately $14 \mu_b/\text{nm}^2$, slightly reduced from the expected saturation magnetization of a single uncompensated layer ($19 \mu_b/\text{nm}^2$).

Importantly for later discussions, we observe a reversal of the direction of the stray field over the narrow 6/8-layer stripe when B_{ext} is increased to 141.5 mT (Fig. 1e). Our simulation (Fig. 1f) and extracted linecut (Supplementary Fig. 1i) explain that this reversal corresponds to the flipping of a single layer that is anti-aligned with the external field, such that the net magnetization of the even-layer stripe increases from approximately fully-compensated to two uncompensated layers ($28 \mu_B/\text{nm}^2$). For the outer even-layer regions (4 and 6-layer), the stray fields at their boundaries become stronger at $B_{ext} = 141.5$ mT, with a weak positive field in the 6-layer’s interior, signaling the emergence of finite magnetizations due to canting of the spins out of the plane.

B. Optical Modulation of Néel Magnetization

Having established the underlying in-plane, layered AF state, we now uncover a startling optical effect on the Néel magnetization of atomically thin CrCl_3 . Figure 2a displays the dc stray field image at $B_{ext} = 141.5$ mT for another CrCl_3 flake containing 5, 6, and 8-layer regions. Significant B_{NV} is again only observed over the odd-layer area.

Using only the green NV probe beam, we switch to a Hahn echo sequence for sensing dynamic fields. Here, the NV center is prepared in a superposition state and allowed to precess over a free evolution time 2τ , separated into two halves by a π -pulse (Fig. 2b). The total precession angle Φ is determined from $\Phi = \arctan(Y_P/X_P)$, where X_P and Y_P are the X- and Y-axis Bloch sphere projections of the final state (Appendix B). If the stray magnetic field is static over the 2τ evolution, the precession during the first half exactly cancels that over the second half, and $\Phi = 0$. This trivial behavior is indeed observed over the bare NV substrate (0-layer), such that Y_P remains fixed at 0 and X_P decays smoothly due to quantum decoherence as the evolution time is lengthened (Fig. 2c). Unexpectedly, when we perform the Hahn echo over the 5-layer region, Y_P displays a pronounced

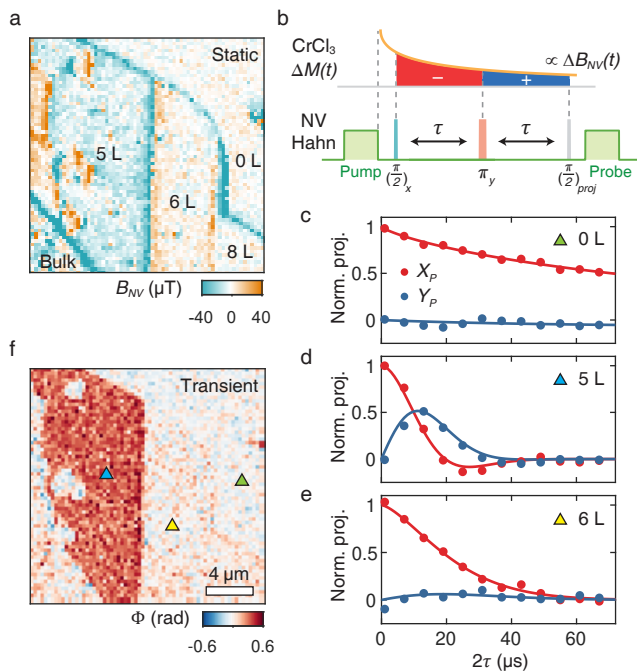


FIG. 2. Transient stray fields from optically-excited CrCl₃. (a) Preliminary: dc stray field (B_{NV}) image identifying 5, 6, 8-layer and bulk regions of a CrCl₃ flake. (b) Schematic of a Hahn echo sequence with total duration 2τ applied to the NV center, alongside a temporally decaying magnetic field $\Delta B_{NV}(t)$ due to a magnetization change $\Delta M(t)$ in CrCl₃ induced by the initial green pulse (power $P = 80 \mu\text{W}$). The π -pulse negates the phase accumulated during the first half of the evolution. (c,d,e) Hahn echo measured over: c) the bare NV substrate (0-layer), d) 5-layer region, and e) 6-layer region. Only the 5-layer region engenders a non-zero NV precession angle Φ , indicated by the simultaneous evolution of the X_P and Y_P projections of the NV superposition state with increasing Hahn echo duration. The solid lines in (c-e) are fits assuming an exponential decoherence envelope and a possible linearly increasing Φ with 2τ (Supplementary Section IV). (f) Image of the precession angle Φ , reflecting the optically-induced transient stray field, for an Hahn echo sequence with $2\tau = 13 \mu\text{s}$ over the same region as (a) by scanning the single green beam ($B_{ext} = 141.5 \text{ mT}$).

increase before being bounded by the decoherence envelope, revealing that the precession angle Φ increases with evolution time (Fig. 2d). The same experiment on the 6-layer region, however, exhibits only faster decoherence compared to the bare substrate due to magnetic fluctuations in CrCl₃, but negligible coherent phase accumulation (Fig. 2e).

By scanning the green beam over the diamond and CrCl₃, we spatially image the accumulated Φ for a Hahn echo sequence with fixed evolution time $2\tau = 13 \mu\text{s}$ (Fig. 2f). We observe nearly homogeneous phase precession over the 5-layer region, but negligible precession over the 6 and 8-layer regions. For particular experimental conditions (e.g., coherence time), this imaging scheme can be significantly faster than ODMR for distinguishing even

and odd layers due its strong signal in the flake's interior, independent of the flake's dimensions, and fewer data points needed per pixel (Appendix B).

Our results clearly indicate that a time-varying magnetization $\Delta M(t)$ is stimulated in the CrCl₃ flake (e.g., a decaying exponential as diagrammed in Fig. 2b), such that its stray field is not constant over the two halves of the Hahn echo. One reasonable, but inconsistent, hypothesis is that NV center probe laser locally heats the CrCl₃ flake, causing a transient demagnetization that gradually recovers during the intervening laser off period. If thermal demagnetization were the mechanism, we would expect Φ to saturate when 2τ significantly exceeds the thermal time constant ($\approx 1 \mu\text{s}$) (Supplementary Section V) [57]. However, the experimental Φ is growing over tens of microseconds (Fig. 2d), indicating a much longer magnetization recovery time. Moreover, we will show that the spatial distribution of the transient stray field corresponds to an *enhancement*, rather than a reduction, of the in-plane magnetization.

C. Pump-Probe Imaging of Locally Enhanced Magnetization

By incorporating a second laser dedicated to pumping CrCl₃, we can scan the NV probe beam while holding the CrCl₃ excitation fixed to map the stray field profile of the optically-induced magnetization. We pulse the pump laser after the NV probe laser has been turned off for at least $50 \mu\text{s}$ to allow the incidental effect of the probe to decay (Fig. 3a). The polarization of the pump laser is linear and does not alter the results. Crucially, the Hahn echo is still required for sensitivity, as dc sensing with the pump laser on cannot resolve the small magnetization difference.

Figure 3b shows images of the transient stray field as a function of temperature upon exciting the 7-layer stripe of Fig. 1a with a pump wavelength $\lambda = 730 \text{ nm}$. The spatially-resolved $\Phi(\mathbf{r})$, where \mathbf{r} denotes the position of the probe beam relative to the pump, displays a double-lobe, sign-switching feature, which remains virtually unchanged up to a few Kelvin below T_N , but disappears at 18 K (above T_N). Notably, the positive lobe (red) in $\Phi(\mathbf{r})$ includes the center point where the pump and probe beams coincide (yellow circle), consistent with the sign for Φ measured when the single NV beam serves as both pump and probe (Fig. 2f).

At $B_{ext} = 141.5 \text{ mT}$, the phase accumulated by our sensing state during the Hahn echo is given by an integral of the transient stray field $\Delta B_{NV}(t)$:

$$\Phi(2\tau, t_d) = 2\pi\gamma_e \left(\int_{t_d+\tau}^{t_d+2\tau} \Delta B_{NV}(t') dt' - \int_{t_d}^{t_d+\tau} \Delta B_{NV}(t') dt' \right). \quad (1)$$

Measurements using a simulated waveform for $\Delta B_{NV}(t)$ corroborate that positive Φ corresponds to ΔB_{NV} that

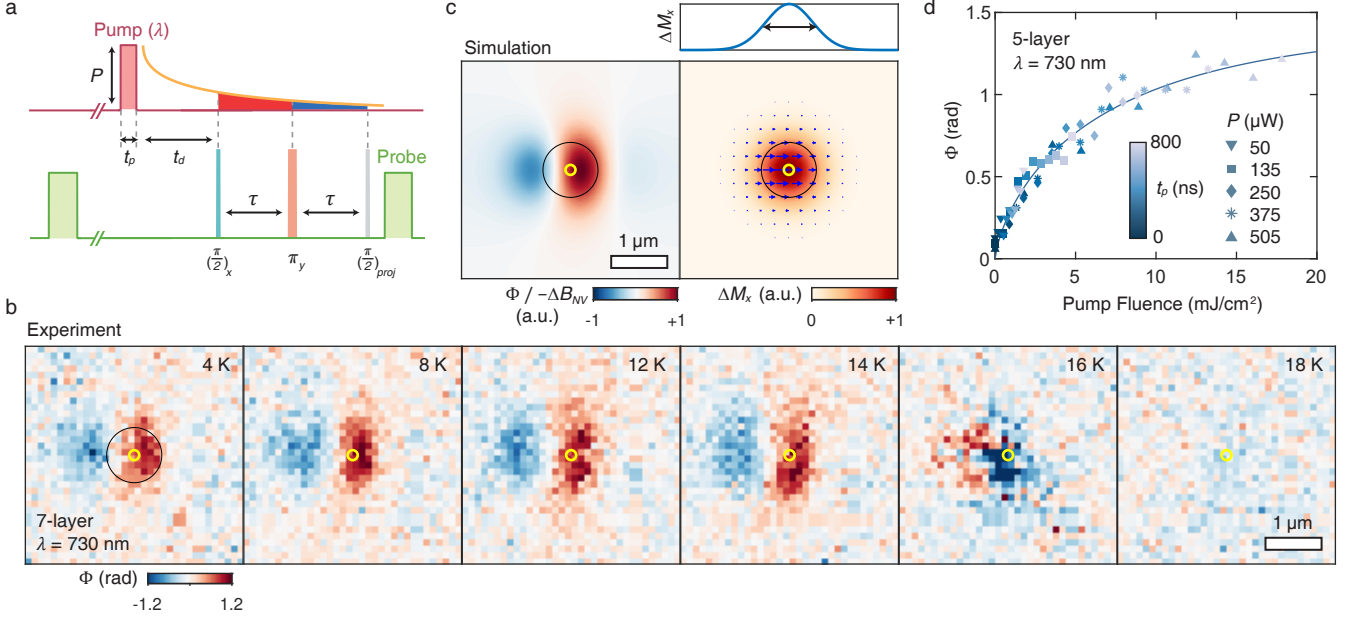


FIG. 3. Pump-probe imaging of exciton-enhanced magnetization. (a) Experimental timeline integrating a pump beam (wavelength λ) into the Hahn echo sequence. The pump pulse of width t_p and power P occurs at least $50 \mu\text{s}$ after the initial green pulse (NV initialization); the Hahn echo is commenced after a delay t_d from the pump pulse. (b) Temperature evolution of the local Hahn precession angle $\Phi(\mathbf{r})$ on a 7-layer region, measured by scanning the probe beam relative to a fixed pump beam at the yellow circle. $\Phi(\mathbf{r})$ images the spatial distribution of the transient stray field induced by the pump beam ($\lambda = 730$ nm, $P = 220 \mu\text{W}$, $t_p = 1.2 \mu\text{s}$, $t_d = 0$, $2\tau = 13 \mu\text{s}$). (c) Left: simulation of the additional stray magnetic field $\Delta B_{NV}(\mathbf{r}) \propto -\Phi(\mathbf{r})$ due to a Gaussian enhancement of the in-plane magnetization $\Delta M_x(\mathbf{r})$. Right: Spatial distribution and linecut of the simulated $\Delta M_x(\mathbf{r})$ with the black circle and double arrow denoting the full width at half maximums. (d) Maximal NV precession angle Φ on a 5-layer CrCl_3 region after a single pump pulse of variable fluence. The fluence is varied by changing either the duration t_p or power P of the pump pulse, with the data collapsing onto a single saturation curve.

is more negative (antiparallel to the NV axis) in the first half of the Hahn echo sequence than in the second half (Supplementary Section V).

The localized pattern for $\Phi(\mathbf{r})$ (Fig. 3b) motivates us to consider a Gaussian profile, following the pump beam intensity, for the optically-induced magnetization $\Delta M(\mathbf{r}, t)$. In Fig. 3c, we simulate the additional stray field $\Delta B_{NV}(\mathbf{r})$ produced by $\Delta M(\mathbf{r})$ corresponding to an enhancement of the in-plane magnetization along the $+\hat{x}$ direction with Gaussian amplitude and full-width-half-maximum of $1.0 \mu\text{m}$ (black circle), approximately the pump beam size. The time-integrated $\Phi(\mathbf{r})$ measured by Hahn echo should then display the same spatial distribution as $-\Delta B_{NV}(\mathbf{r})$ since $\Delta B_{NV}(\mathbf{r}, t)$ decays towards zero during the echo duration (Eq. 1). Fig. 3d displays the typical dependence of the maximal Φ on the pump fluence, showing it to saturate for high powers P or long pulse widths t_p , hinting at a metastable state whose population can saturate.

The excellent correspondence between the experimental (Fig. 3b) and simulated patterns (Fig. 3c) demonstrates that below T_N , the existing in-plane magnetization is locally enhanced by optical excitation. Alternatively, we can allow the Gaussian enhancement $\Delta M(\mathbf{r})$ to be oriented along an arbitrary angle θ_m in the xz -

plane (Supplementary Fig. 3). In this analysis, $\theta_m \approx 0^\circ$ ($+\hat{x}$) still produces the best fit to the experimental $\Phi(\mathbf{r})$ image. To explain the even-odd contrast in the observable ΔB_{NV} (Fig. 2f), we plausibly suppose that the enhancement ΔM in each CrCl_3 layer, if any, occurs along the magnetization direction of that layer. Then ΔB_{NV} would be canceled over even layer areas due to AF interlayer coupling, although the underlying effect occurs everywhere.

As T_N is approached upon warming to 16 K, the $\Phi(\mathbf{r})$ pattern nearly inverts for this specific flake (Fig. 3b). A higher resolution temperature sweep for a different 7-layer flake, presented in Supplementary Fig. 5, shows a rapid series of changes in $\Phi(\mathbf{r})$, including progressive rotations of its symmetry axis, near T_N . The symmetry axis of $\Phi(\mathbf{r})$ reflects the vector direction of the transient change in magnetization. For example, we can deliberately rotate $\Phi(\mathbf{r})$ by adding a vertical (\hat{y}) component to the bias field B_{ext} (Supplementary Fig. 6), which rotates the static magnetization of CrCl_3 given its negligible intrinsic anisotropy within the easy plane. Hence, the fickle patterns in $\Phi(\mathbf{r})$ near criticality could relate to local fluctuations in anisotropy, or to other potential subtleties such as laser heating (demagnetization) or inhomogeneous Néel temperature T_N [58].

D. Role of Strongly Bound Excitons

We focus our attention to understanding the robust magnetization enhancement below T_N by studying its dependence on the CrCl_3 excitation wavelength. Fig. 4a shows $\Phi(\mathbf{r})$ imaged on a 9-layer flake at six different pump wavelengths λ between 405 nm and 785 nm. These wavelengths all lie below the ligand-metal charge-transfer absorption edge for CrCl_3 at 3.2 eV (388 nm) [59]. To mitigate photon noise associated with excitation of the NV center for $\lambda < 637$ nm (e.g. Fig. 4b), we use a nonzero delay $t_d = 1 \mu\text{s}$ for all λ , which allows some fraction of the excited NV centers to relax prior to sensing. This NV charge noise cannot bias the pattern for $\Phi(\mathbf{r})$, since the coherent signal is contributed only by NV centers present in the correct, microwave-addressable ground state at the start of the Hahn echo. For each λ , we fit $\Phi(\mathbf{r})$ according to the Gaussian model (Fig. 3c) with the beam width and amplitude ΔM_x of the magnetization enhancement along the \hat{x} -direction as free parameters. Figure 4c shows the extracted ΔM_x as a function of λ , normalized by the highest enhancement at $\lambda = 730$ nm. In the same figure, we overlay the optical absorption spectrum of CrCl_3 calculated from data at 4.2 K in Ref. [60], showing it to mimic the wavelength dependence of the optical magnetization enhancement.

The prominent absorption peaks at ~ 1.7 eV and ~ 2.4 eV correspond to the two lowest energy bright excitons (X_1 and X_2) identified in recent many-body perturbation theory calculations of CrCl_3 excited states [25, 27]. These excitons derive from the interconfigurational $d-d$ transitions of the Cr^{3+} ion ($3d^3$) in an octahedral ligand field that become parity-allowed due to metal-ligand hybridization. The latter dp -hybridization increases with halogen size; hence, excitons in CrCl_3 are expected to be the darkest and most tightly bound, while they are the brightest and most delocalized in CrI_3 [5, 25].

To clarify the role of excitons, we compare the lifetime of the optically-induced magnetization τ_m to the exciton lifetime τ_{opt} . In Fig. 5a, we visualize the decay of $\Phi(\mathbf{r})$ for increasing delay t_d between the pump pulse and Hahn echo sequence on a 7-layer region. To quantitatively extract τ_m , we park the probe at the position of highest intensity in $\Phi(\mathbf{r})$ (yellow cross in Fig. 5a) and measure the acquired Φ as a function of both the delay t_d and total evolution time 2τ (Fig. 5b). We then use Eq. 1 to simultaneously fit this set of curves, assuming a phenomenological form of the magnetization decay $\Delta M(t) = \Delta M_0 \exp(-(t/\tau_m)^\alpha)$ that creates $\Delta B(t)$ through the Gaussian model (Supplementary Section VI). The best-fit $\Delta M(t)$ curve is plotted in Fig. 5c, displaying an estimated magnetization lifetime $\tau_m = 26 \pm 3 \mu\text{s}$ with exponent $\alpha = 0.5 \pm 0.1$ and a maximal magnetization change $\Delta M_0 = 0.46 \pm 0.1 \mu_B/\text{nm}^2$.

In contrast, the time-resolved PL intensity for a representative 7-layer CrCl_3 flake (Fig. 5d), isolated with a 800 nm long-pass filter [46], completely decays within 1 μs , indicating an exciton lifetime $\tau_{opt} \approx 40$ ns for 515 nm

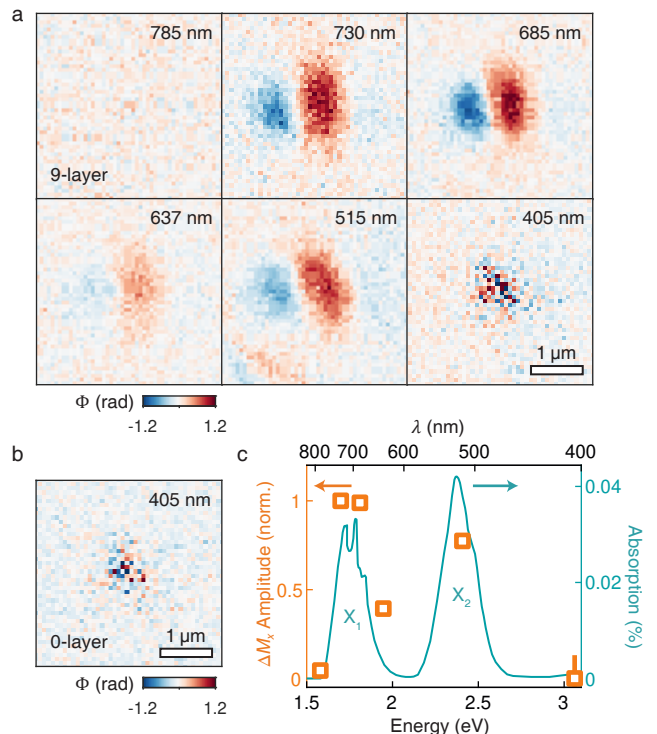


FIG. 4. Dependence of ΔM_x on the pump wavelength λ . (a) Dual-beam Hahn echo phase maps $\Phi(\mathbf{r})$ imaged on a 9-layer region for six different λ ($t_d = 1 \mu\text{s}$, $2\tau = 20 \mu\text{s}$). The optical power P is 180 μW , except for $\lambda = 405$ nm, where $P = 55 \mu\text{W}$. For $\lambda < 637$ nm, the pump beam can excite or ionize the NV center, but this introduces only incoherent photon noise, as visible in the $\lambda = 405$ nm image. (b) $\Phi(\mathbf{r})$ imaged on bare diamond with pump $\lambda = 405$ nm, showing that the speckle noise is due to NV ionization and independent of CrCl_3 . (c) Orange data points: extracted magnetization enhancement amplitude ΔM_x (normalized by $\lambda = 730$ nm and for power P) versus the pump wavelength λ . The overlaid teal curve denotes the expected optical absorption for a 9-layer flake, revealing two exciton peaks X_1 and X_2 (absorption data derived from Ref. [60]).

excitation (X_2). Since τ_{opt} is two orders of magnitude shorter than τ_m , the exciton itself cannot be the magnetically enhanced state, but rather must give rise to the latter during its recombination as a long-lived intermediate state.

As excitons in CrCl_3 are nearly radiatively forbidden, we anticipate that nonradiative recombination could present the primary limit to τ_{opt} . In Fig. 5e, we display the PL intensity normalized by the number of layers at 730 nm excitation (X_1) for several CrCl_3 regions between 2 to 11 layers thick. The red (blue) data points denote regions encapsulated (not encapsulated) by hBN, where both samples were prepared in the glovebox and simultaneously loaded into the cryostat. Although we observe variations among regions of identical thickness, the PL *per layer* for both conditions decreases for thinner flakes, a trend similar to CrI_3 [5]. Simultaneously, the

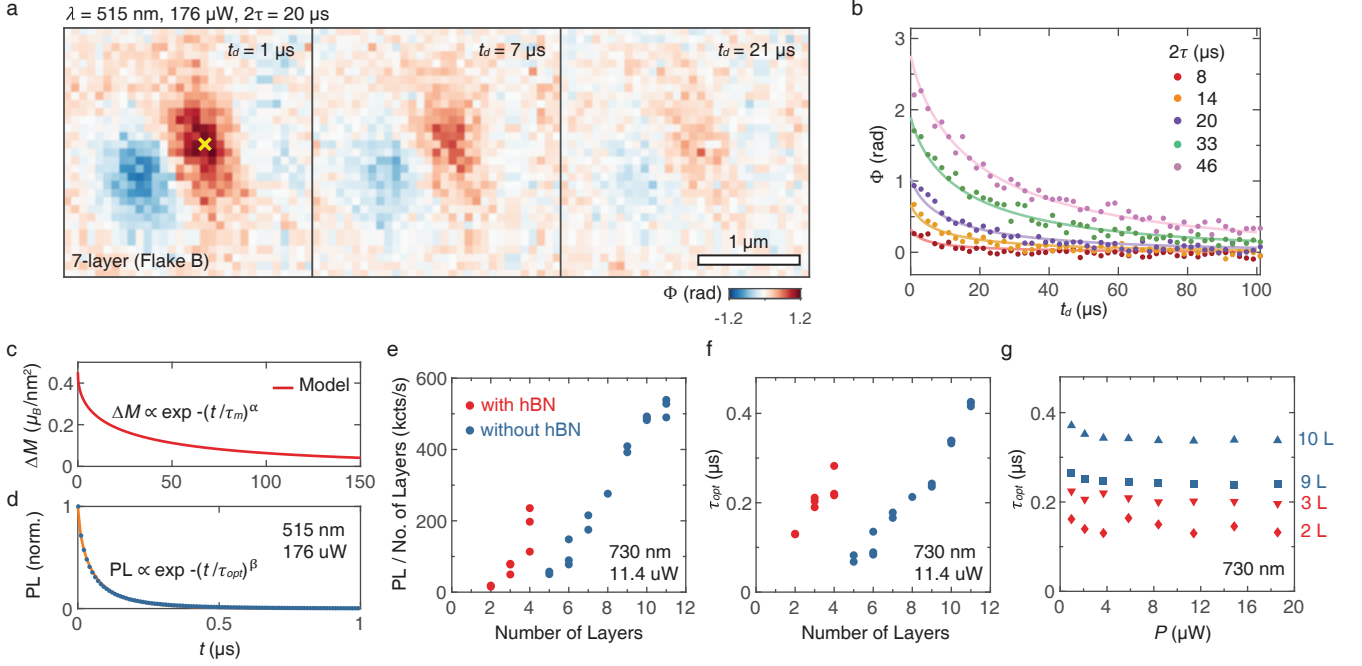


FIG. 5. Time-resolved magnetization and PL measurements. (a) Spatiotemporal images of $\Phi(\mathbf{r})$ for various delays t_d between the pump pulse and Hahn echo sequence on 7-layer CrCl_3 . The rotation of the $\Phi(\mathbf{r})$ symmetry axis away from the $+x$ -direction here is atypical for 4 K and likely reflects a local in-plane anisotropy that competes with the external field B_{ext} . (b) Hahn echo phase Φ measured at the yellow cross in a) as a function of the pump-probe delay t_d and total echo duration 2τ . The solid lines are simultaneous best fit curves using a magnetization decay model $\Delta M(t) = \Delta M_0 \exp(-(t/\tau_m)^\alpha)$. (c) Inferred magnetization decay from b), yielding $\Delta M_0 = 0.46 \mu_B/\text{nm}^2$, $\tau_m = 26 \mu\text{s}$, and $\alpha = 0.5$. (d) Decay of the PL intensity for 7-layer CrCl_3 after excitation with $\lambda = 515 \text{ nm}$ (X_2). The solid best fit line extracts a long exciton lifetime $\tau_{opt} = 38 \text{ ns}$ and exponent $\beta = 0.6$. (e) PL intensity per layer versus number of CrCl_3 layers for $\lambda = 730 \text{ nm}$ excitation (X_1). (f) Exciton lifetime τ_{opt} versus number of CrCl_3 layers for $\lambda = 730 \text{ nm}$, with $\beta = 0.79$ fixed for all. (g) Dependence of τ_{opt} on the excitation power P for selected layer thicknesses. The red (blue) points in e), f), g) denote data from regions encapsulated (not encapsulated) by hBN.

exciton lifetime τ_{opt} is reduced with decreasing thickness (Fig. 5f), with flakes lacking hBN encapsulation having shorter lifetimes and lower PL for comparable thickness. Taken together, Figs. 5e,f clearly identify the rise of nonradiative transitions, as opposed to diminishing radiative oscillator strength, as the primary mechanism for PL quenching in thinner layers.

Our evidence that exciton pumping creates an alternative magnetically enhanced electronic state hints that the energy dissipated in nonradiative exciton recombination may be transferred to a nearby electronic carrier, a channel known as Auger recombination. Moreover, the sensitivity of τ_{opt} to layer thickness and surface encapsulation (Fig. 5f) implies that Auger recombination in CrCl_3 is catalyzed by defects residing in the surface layers. Excitons produced in the bulk can hop between layers [61] within a finite diffusion length to reach the surface, where the recombination rate is highest. The rate for defect-assisted Auger recombination crucially depends on the probability of finding the exciton's electron and hole near each other, and hence should be strongly enhanced in CrCl_3 with its near-atomic exciton radii [32, 33]. The conventional Auger process for delocalized Wannier-Mott excitons in narrow bandgap semiconductors is instead

governed by exciton-exciton collisions, resulting in an exciton lifetime that is inversely proportional to the square of the exciton density in the high-density limit [62]. In contrast, Fig. 5g shows that the lifetime τ_{opt} in few-layer CrCl_3 is independent of the optical excitation power, assumed to be proportional to the exciton density. This independence from the exciton density is a direct signature of defect-assisted Auger recombination of single localized excitons [32, 33].

E. Controllable, Surface-Sensitive Magnetization Enhancement

We next demonstrate that the optically-induced magnetization is surface-dominated and sensitive to surface condition. First, for the 6/8-layer stripe of Fig. 1 at high B_{ext} , we observe a dc stray field that is approximately twice as strong as its neighboring odd-layer regions (Fig. 1e), indicating an extra flipped layer in its volume. However, its transient stray field under exciton pumping is virtually identical in strength to the nearby odd-layer regions (Hahn map, Fig. 6a). This is explained if the surface monolayers dominate the contribution to the op-

tical enhancement since if all layers contributed equally, the transient signal would also be twice as strong. Indeed, the flipped layer in the 6/8-layer stripe is expected to be a surface layer, since this configuration minimizes the energy penalty for breaking AF interlayer exchange.

Second, we fabricate another CrCl_3 flake where we deliberately encapsulate only a portion of the flake with hBN. This allows an unequivocal comparison of the surface condition by ensuring that the same starting sample experiences identical exposures inside the glovebox and in ambient during sample loading. In Fig. 6b, we plot the PL of the CrCl_3 flake on diamond using a logarithmic colorbar to emphasize thinner regions. Areas of the same layer thickness are significantly dimmer when not encapsulated by hBN, corroborating the role of surface defects in promoting nonradiative exciton recombination (Fig. 5e,f.).

Figure 6c displays the static stray field (B_{NV}) image of the same flake, showing that antiferromagnetic interlayer coupling is retained down to three layers. Strikingly, the transient stray field image obtained under exciton pumping with the single green beam displays a prominent contrast between the exposed and covered regions (Fig. 6d). The average Hahn echo phase Φ recorded over the exposed portion of the odd-layer stripes increases by more than a factor of two over the hBN covered portion ($\Phi_{\text{exposed}} \approx 0.60$ rad, $\Phi_{\text{covered}} \approx 0.25$ rad), excluding a transitional region near the termination of the hBN. This comparison pinpoints environmentally-induced defects in the surface layers as the common catalyst for optically-enhanced magnetization (Fig. 6d) and nonradiative exciton recombination (Fig. 6b).

To probe the origin of the surface defect responsible for these simultaneous effects, we expose a few-layer CrCl_3 flake to controlled doses of water vapor or oxygen gas, the two main reactive species residual in our glovebox and in ambient. Fig. 7a presents the initial transient field image $\Phi(\mathbf{r})$ for the sample, again partially-covered by hBN. A baseline level for Φ is measured despite minimized sample preparation (3 hours in glovebox) and transfer time (110 seconds in ambient). After thermal cycling the sample without pumping, we then deliberately expose the surface to 200 mBarr of O_2 gas for 3 minutes at room temperature (290 K). This treatment increases Φ by ≈ 0.2 radians in the both the exposed and encapsulated regions (Fig. 7b), indicating that single-sided encapsulation does not form a gas-tight seal [63]. When our cryostat is warmed up without pumping, a pressure of approximately $5 \cdot 10^{-2}$ mBarr is measured after crossing 273 K, which is dominated by outgassed H_2O molecules. Residual gas analysis indicates the ratio of H_2O to O_2 in this state is 160:1. Hence, although this first iteration demonstrates control over the surface defect density and the amplitude of the transient magnetization, it does not yet distinguish between H_2O or O_2 exposure as the cause.

We perform a second thermal cycle where we instead continuously pump on the cryostat during warming, which limits the evolved H_2O pressure to $< 1 \cdot 10^{-4}$

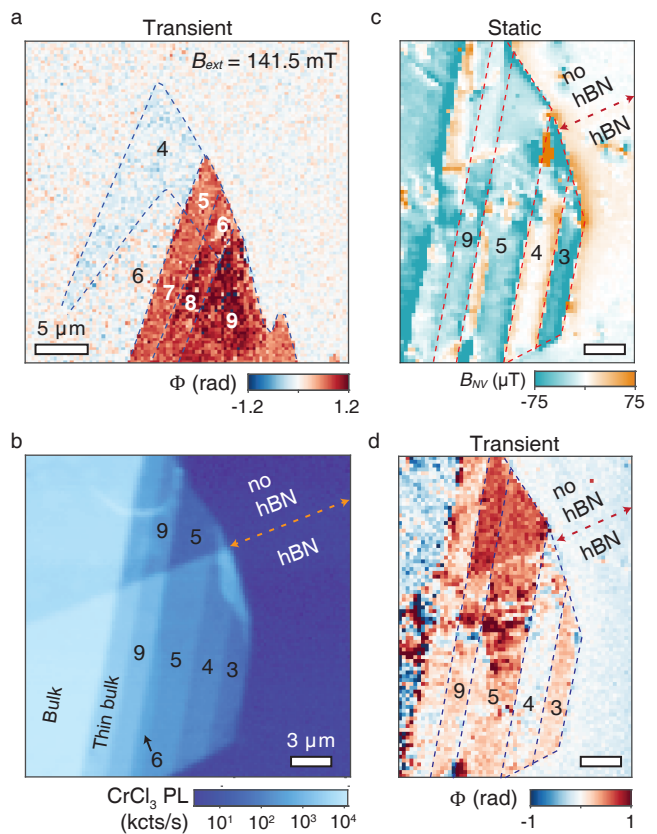


FIG. 6. Surface-sensitive magnetization enhancement. (a) Hahn image for the 4-9 layer CrCl_3 flake (hBN encapsulated) of Fig. 1 at high $B_{\text{ext}} = 141.5$ mT. The Hahn precession angle Φ with $2\tau = 13 \mu\text{s}$ is measured as the single green beam (515 nm) is rastered over the flake. The amplitude of the transient field over the 6/8-layer stripe is similar to the neighboring odd-layer regions even though the former possesses a twice larger volume magnetization. (b) PL image (>800 nm) for a 3-9 layer CrCl_3 flake with partial hBN encapsulation. The edge of the hBN cuts across the entire flake parallel to the dashed orange line. The PL is quenched over unencapsulated regions due to defect-assisted, nonradiative exciton recombination. (c) Static stray field (B_{NV}) image of the same flake confirming even-odd layer parity and displaying slightly reduced stray fields over the unencapsulated area. (d) Hahn image of the same flake with $2\tau = 19 \mu\text{s}$. The transient stray field, proportional to Φ , strongly increases in the exposed areas of the odd-layer stripes, indicating that surface impurities catalyze the optical magnetization enhancement.

mBarr (brief spike near 273 K). We then quickly dose the surface again with 200 mBarr of O_2 for 3 minutes (Fig. 7c). In this case, the sample experiences only exposure to O_2 , and no change in Φ is observed. To confirm this result, we repeat the thermal cycle under pumping and expose the sample to an additional 9 minutes of O_2 (Fig. 7d). The measured transient field Φ actually slightly decreases after this treatment, indicating that O_2 exposure may displace the actual active surface impurity. In contrast, exposing CrCl_3 to only H_2O by a final ther-

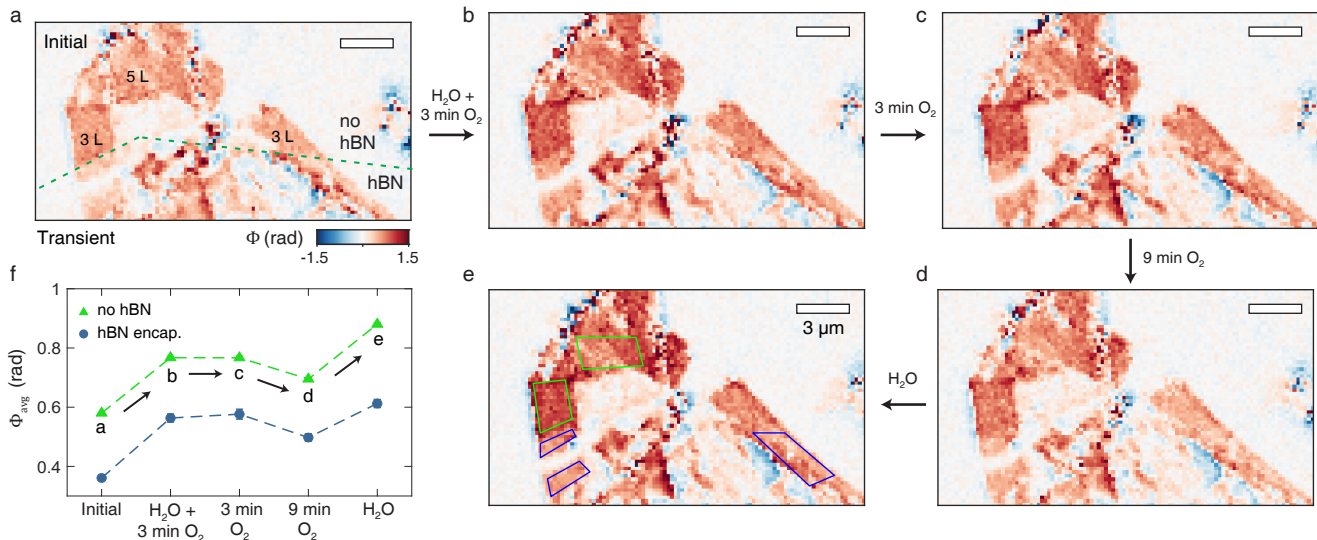


FIG. 7. Magnetization enhancement under controlled gas exposure. (a) Initial Φ image (single beam, $\lambda = 515 \text{ nm}$, $P = 50 \mu\text{W}$, $2\tau = 19 \mu\text{s}$) for an as transferred flake, containing 3 and 5-layer regions. The edge of the hBN encapsulation is delineated by the green dashed line. (b) Φ image after thermal cycling the sample without pumping (equivalent to H_2O exposure at $5 \cdot 10^{-2} \text{ mBar}$ for approximately 2 hours) and then exposing it to 200 mBar pure O_2 gas for 3 minutes. (c) Additional exposure to only O_2 (200 mBar, 3 minutes). Here, the sample was thermal cycled under continuous pumping to limit H_2O pressures below $1 \cdot 10^{-4} \text{ mBar}$. (d) Additional exposure to only O_2 (200 mBar, 9 minutes). (e) Additional exposure to only H_2O (thermal cycling without pumping). (f) Summary of the evolution of Φ versus sequential surface treatment. The green (blue) data denotes Φ over the exposed (encapsulated) regions of the flake as determined by the average over the regions defined by the matching colored boxes shown in (e). The transient magnetization enhancement, proportional to Φ , increases after exposure to H_2O , but not O_2 .

mal cycle without pumping and with no introduction of O_2 increases Φ once more (Fig. 7e). The evolution of Φ after sequential surface treatments is summarized in Fig. 7f and definitively proves that H_2O exposure, rather than O_2 , provides the dominant catalyst for our effect.

F. Defect-Assisted Exciton Recombination Mechanism

The experimental signatures thus point toward the following defect-assisted Auger recombination mechanism [32, 33] to stimulate the optically-enhanced magnetization in atomically thin CrCl_3 . Auger recombination of excitons is mediated by an H_2O -induced surface impurity, which introduces an occupied mid-gap level. During recombination, this defect level captures the hole of the exciton and transfers the excess energy to its electron partner, injecting it into the spin-polarized conduction band (Fig. 8a, middle). This effectively converts an unpolarized defect electron into a spin-up conduction electron, increasing the system magnetization by $\approx 1\mu_B$ per event. To conserve total angular momentum, phonons generated by localized vibrations of the defect state must also participate in the recombination [64]. Finally, the resulting excited state persists until the ionized defect level recaptures an electron from the conduction band (Fig. 8a, right), which is accompanied by multi-phonon

emission and results in the slow magnetization recovery time τ_m observed at cryogenic temperatures.

For monolayer CrI_3 , electron doping via halogen vacancies [34, 36] or metal adsorption [37, 38] has indeed been proposed to increase the electron charge (from $3d^3$ to $3d^4$) and magnetic moment of the Cr ion, since a high spin configuration is preferred for the weak Cl ligand field. In the band picture, this amounts to partial filling of the lowest energy, majority-spin conduction bands contributed primarily by the Cr e_g orbitals. In our mechanism, we realize this doping effect in the surface monolayers of CrCl_3 through optically inducing charge transfer from surface impurities. Since the surface monolayers of CrCl_3 dominate the magnetization enhancement, an even-odd effect is naturally produced: in odd-layer (even-layer) regions, the top and bottom layers have parallel (anti-parallel) magnetizations. Assuming that $\Delta M_0 \approx 0.5 \mu_B/\text{nm}^2$ is contributed equally by the two surfaces, an excess electron density of $2.5 \cdot 10^{13}/\text{cm}^2$ is induced locally inside the beam spot in each surface monolayer, which is comparable to levels achieved by electrostatic doping of CrI_3 [65]. In the latter experiment, complementary signatures to enhanced magnetization, such as enhanced coercive fields and critical temperatures, were also observed [65].

To quantitatively evaluate the plausibility of defect-assisted Auger recombination, we turn to DFT calculations. For a pristine CrCl_3 surface, we find that the adsorption energy for an H_2O molecule ($E_{ads} = -0.15 \text{ eV}$)

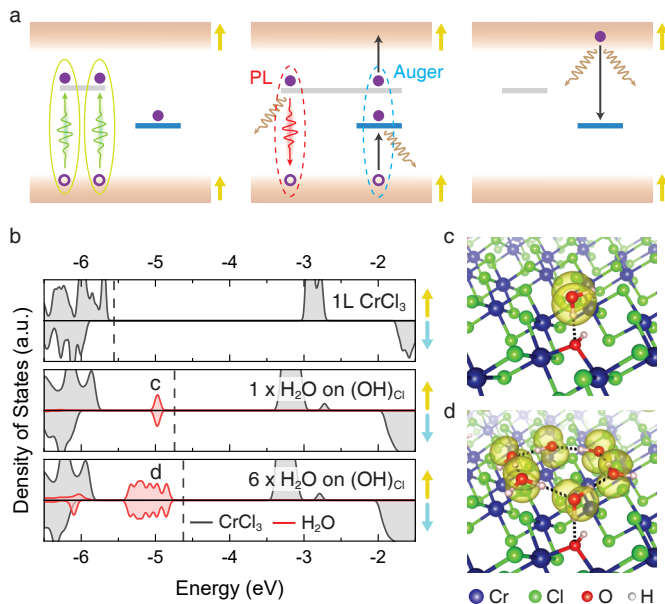


FIG. 8. Proposed mechanism for magnetization enhancement through defect-assisted Auger recombination. (a) Mechanism. Left: near-resonant excitation of CrCl_3 creates strongly bound excitons (filled circle - electron, open circle - hole). An in-gap defect state is occupied. Center: Excitons can recombine radiatively, resulting in PL (red), or nonradiatively through defect-assisted Auger recombination (blue). The three-particle Auger process converts, in effect, an unpolarized defect electron into a spin-up CrCl_3 conduction electron. Phonons (brown arrows) can participate in both radiative and Auger recombination. Right: the excited state after Auger recombination decays by multi-phonon emission and electron capture by the ionized defect. (b) Spin-resolved density of states for a pristine CrCl_3 monolayer (top); a monolayer with a single H_2O molecule adsorbed onto $(\text{OH})_{\text{Cl}}$, denoting an $-\text{OH}$ group that substitutes for a Cl atom (middle); a monolayer with six H_2O molecules adsorbed onto $(\text{OH})_{\text{Cl}}$ (bottom). Gray (red) lines indicate the contributions from monolayer CrCl_3 (H_2O). The Fermi level is shown as the vertical dashed line. (c,d) Spatial spin distributions, doubly degenerate, for the localized, in-gap states labeled in (b), contributed by a single H_2O adsorbate and a cluster of six H_2O adsorbates, respectively. The dashed lines denote hydrogen bonds.

is greater than the Gibbs free energy of gas-phase H_2O at ambient conditions ($E_{\text{gas}} \approx -0.5$ eV) [66]; hence, direct physisorbed H_2O should be thermodynamically unfavorable (Supplementary Sec. VIII). However, Cl vacancies are known to be prevalent in CrCl_3 [67]. The excess electron density near this vacancy may provide a natural site for hydrolysis and the binding of an $-\text{OH}$ group, forming a substitutional $(\text{OH})_{\text{Cl}}$ defect. Subsequent H_2O molecules will form hydrogen bonds to the randomly distributed $-\text{OH}$ groups and thereafter to each other for greater stability. As a concrete, but arbitrary example, a ring configuration of six H_2O molecules hydrogen-bonded around a single $(\text{OH})_{\text{Cl}}$ (Fig. 8d) is found to possess $E_{\text{ads}} = -0.47$ eV per molecule. Thus, Cl vacancies pro-

vide attachment points to nucleate the growth an H_2O adsorbate layer, whose presence has been deduced from surface science experiments [68, 69].

Fig. 8a (top) presents our DFT calculation of the spin-resolved, projected density of states for CrCl_3 , displaying majority-spin valence and conduction bands near the Fermi level. A single H_2O molecule adsorbed at $(\text{OH})_{\text{Cl}}$ introduces a spin-degenerate defect state inside the CrCl_3 band gap (Fig. 8b, middle). The spin-up density for this state (identical to spin-down) is depicted in Fig. 8c, showing it to derive primarily from the nonbonding oxygen p -orbital that is perpendicular to the H_2O molecule plane. For the six H_2O cluster, the in-gap state broadens into a defect band due to orbital hybridization (Fig. 8b, bottom). These in-gap levels should appear generically for a disordered, weakly bonded H_2O layer and could plausibly mediate Auger recombination of excitons. They are theoretically predicted to be energetically situated closer to the valence band for efficient hole capture, while also being within ~ 1.7 eV of the conduction band to allow the X_1 exciton to scatter an electron into it. Alternatively, we find that O_2 -related defects and intrinsic vacancy defects do not provide appropriate conditions for optical magnetization enhancement (Supplementary Sec. VIII). The former possess large formation energies, making them thermodynamically unfavorable. The latter vacancy defects introduce spin-majority in-gap states that already increase the magnetization of CrCl_3 without optical excitation, and moreover, their density should be unchanged by our gentle gas exposures.

G. Conclusions

We have revealed that exciton pumping enhances the in-plane, layer-alternating magnetization of atomically-thin CrCl_3 . Experimental and theoretical evidences support a mechanism where the Auger recombination of strongly bound excitons in the surface layers activates charge transfer between water-induced adsorbates and the Cr majority-spin bands. Through an innovative quantum coherent sensing protocol, our work demonstrates that impurities can enhance the intrinsic magnetism in single atomic layers [34–39]. Exciton-mediated charge transfer may be applicable to diverse semiconducting 2D magnets, including intrinsic Cr- and Mn-based compounds and magnetically-doped TMDs, where long-range order in the latter are still under debate. These systems, including CrX_3 [8, 9, 25–27], CrPS_4 [70], MnPX_3 [71], Fe-doped MoS_2 [72] and V-doped WSe_2 monolayers [73], all harbor tightly bound excitons, either due to nearly forbidden d - d transitions or to reduced dielectric screening, and are susceptible to deep-level states. Indeed, our study opens strategies for future efforts to optimize the magnetization enhancement by extending to bulk layers via doping, intercalation, or defect creation through irradiation.

Optical control is furthermore attractive as a high-

bandwidth knob to modulate the resonant coupling between 2D spin ensembles and small mode volume superconducting resonators for solid-state quantum memory applications [74, 75]. Conventionally achieved by pulsing an external magnetic flux, tuning the magnon resonances and microwave resonator in and out of match could alternatively be realized with fast and focusable pulses of light

that change the magnetization and internal field of the 2D spin ensemble [76, 77]. Finally, further development of the introduced pump-probe quantum magnetometry technique to extend its sensitivity and spatiotemporal resolution could open a new window into light-induced transient magnetism, superconductivity [78], and charge dynamics in condensed matter systems.

-
- [1] B. Huang, G. Clark, E. Navarro-Moratalla, D. R. Klein, R. Cheng, K. L. Seyler, D. Zhong, E. Schmidgall, M. A. McGuire, D. H. Cobden, W. Yao, D. Xiao, P. Jarillo-Herrero, and X. Xu, Layer-dependent ferromagnetism in a van der Waals crystal down to the monolayer limit, *Nature* **546**, 270 (2017).
- [2] C. Gong, L. Li, Z. Li, H. Ji, A. Stern, Y. Xia, T. Cao, W. Bao, C. Wang, Y. Wang, Z. Q. Qiu, R. J. Cava, S. G. Louie, J. Xia, and X. Zhang, Discovery of intrinsic ferromagnetism in two-dimensional van der Waals crystals, *Nature* **546**, 265 (2017).
- [3] Z. Zhang, J. Shang, C. Jiang, A. Rasmita, W. Gao, and T. Yu, Direct Photoluminescence Probing of Ferromagnetism in Monolayer Two-Dimensional CrBr₃, *Nano Letters* **19**, 3138 (2019).
- [4] M. Grzeszczyk, S. Acharya, D. Pashov, Z. Chen, K. Vaklinova, M. van Schilfgaarde, K. Watanabe, T. Taniguchi, K. S. Novoselov, M. I. Katsnelson, and M. Koperski, Strongly Correlated Exciton-Magnetization System for Optical Spin Pumping in CrBr₃ and CrI₃, *Advanced Materials* **35**, 2209513 (2023).
- [5] K. L. Seyler, D. Zhong, D. R. Klein, S. Gao, X. Zhang, B. Huang, E. Navarro-Moratalla, L. Yang, D. H. Cobden, M. A. McGuire, W. Yao, D. Xiao, P. Jarillo-Herrero, and X. Xu, Ligand-field helical luminescence in a 2D ferromagnetic insulator, *Nature Physics* **14**, 277 (2018).
- [6] X. Wang, J. Cao, Z. Lu, A. Cohen, H. Kitadai, T. Li, Q. Tan, M. Wilson, C. H. Lui, D. Smirnov, S. Sharifzadeh, and X. Ling, Spin-induced linear polarization of photoluminescence in antiferromagnetic van der Waals crystals, *Nature Materials* **20**, 964 (2021).
- [7] N. P. Wilson, K. Lee, J. Cenker, K. Xie, A. H. Dismukes, E. J. Telford, J. Fonseca, S. Sivakumar, C. Dean, T. Cao, X. Roy, X. Xu, and X. Zhu, Interlayer electronic coupling on demand in a 2D magnetic semiconductor, *Nature Materials* **20**, 1657 (2021).
- [8] M. Wu, Z. Li, T. Cao, and S. G. Louie, Physical origin of giant excitonic and magneto-optical responses in two-dimensional ferromagnetic insulators, *Nature Communications* **10**, 2371 (2019).
- [9] A. Molina-Sánchez, G. Catarina, D. Sangalli, and J. Fernández-Rossier, Magneto-optical response of chromium trihalide monolayers: chemical trends, *Journal of Materials Chemistry C* **8**, 8856 (2020).
- [10] J. Choi, C. Lane, J.-X. Zhu, and S. A. Crooker, Asymmetric magnetic proximity interactions in MoSe₂/CrBr₃ van der Waals heterostructures, *Nature Materials* **22**, 305 (2023).
- [11] V. Ortiz Jimenez, Y. T. H. Pham, M. Liu, F. Zhang, Z. Yu, V. Kalappattil, B. Muchharla, T. Eggers, D. L. Duong, M. Terrones, and M. Phan, Light-Controlled Room Temperature Ferromagnetism in Vanadium-Doped Tungsten Disulfide Semiconducting Monolayers, *Advanced Electronic Materials* **7**, 2100030 (2021).
- [12] P. Zhang, T.-F. Chung, Q. Li, S. Wang, Q. Wang, W. L. B. Huey, S. Yang, J. E. Goldberger, J. Yao, and X. Zhang, All-optical switching of magnetization in atomically thin CrI₃, *Nature Materials* **21**, 1373 (2022).
- [13] X. Wang, C. Xiao, H. Park, J. Zhu, C. Wang, T. Taniguchi, K. Watanabe, J. Yan, D. Xiao, D. R. Gamelin, W. Yao, and X. Xu, Light-induced ferromagnetism in moiré superlattices, *Nature* **604**, 468 (2022).
- [14] K. Hao, R. Shreiner, A. Kindseth, and A. A. High, Optically controllable magnetism in atomically thin semiconductors, *Science Advances* **8**, eabq7650 (2022).
- [15] M. Dabrowski, S. Guo, M. Strungaru, P. S. Keatley, F. Withers, E. J. G. Santos, and R. J. Hicken, All-optical control of spin in a 2D van der Waals magnet, *Nature Communications* **13**, 5976 (2022).
- [16] G. M. Diederich, J. Cenker, Y. Ren, J. Fonseca, D. G. Chica, Y. J. Bae, X. Zhu, X. Roy, T. Cao, D. Xiao, and X. Xu, Tunable interaction between excitons and hybridized magnons in a layered semiconductor, *Nature Nanotechnology* **18**, 23 (2023).
- [17] Y. J. Bae, J. Wang, A. Scheie, J. Xu, D. G. Chica, G. M. Diederich, J. Cenker, M. E. Ziebel, Y. Bai, H. Ren, C. R. Dean, M. Delor, X. Xu, X. Roy, A. D. Kent, and X. Zhu, Exciton-coupled coherent magnons in a 2D semiconductor, *Nature* **609**, 282 (2022).
- [18] J.-X. Qiu, C. Tzschaschel, J. Ahn, A. Gao, H. Li, X.-Y. Zhang, B. Ghosh, C. Hu, Y.-X. Wang, Y.-F. Liu, D. Bérubé, T. Dinh, Z. Gong, S.-W. Lien, S.-C. Ho, B. Singh, K. Watanabe, T. Taniguchi, D. C. Bell, H.-Z. Lu, A. Bansil, H. Lin, T.-R. Chang, B. B. Zhou, Q. Ma, A. Vishwanath, N. Ni, and S.-Y. Xu, Axion optical induction of antiferromagnetic order, *Nature Materials* **22**, 583 (2023).
- [19] M. McGuire, Crystal and Magnetic Structures in Layered, Transition Metal Dihalides and Trihalides, *Crystals* **7**, 121 (2017).
- [20] C. A. Occhialini, Y. Tseng, H. Elnaggar, Q. Song, M. Blei, S. A. Tongay, V. Bisogni, F. M. F. de Groot, J. Pelliciari, and R. Comin, Nature of excitons and their ligand-mediated delocalization in nickel dihalide charge-transfer insulators, *Physical Review X* **14**, 031007 (2024).
- [21] S. Kang, K. Kim, B. H. Kim, J. Kim, K. I. Sim, J.-U. Lee, S. Lee, K. Park, S. Yun, T. Kim, A. Nag, A. Walters, M. Garcia-Fernandez, J. Li, L. Chapon, K.-J. Zhou, Y.-W. Son, J. H. Kim, H. Cheong, and J.-G. Park, Coherent many-body exciton in van der Waals antiferromagnet NiPS₃, *Nature* **583**, 785 (2020).
- [22] M. Birowska, P. E. Faria Junior, J. Fabian, and J. Kunstmann, Large exciton binding energies in MnPS₃ as a case study of a van der Waals layered magnet, *Physical*

- Review B **103**, L121108 (2021).
- [23] C. A. Belvin, E. Baldini, I. O. Ozel, D. Mao, H. C. Po, C. J. Allington, S. Son, B. H. Kim, J. Kim, I. Hwang, J. H. Kim, J.-G. Park, T. Senthil, and N. Gedik, Exciton-driven antiferromagnetic metal in a correlated van der Waals insulator, *Nature Communications* **12**, 4837 (2021).
- [24] D. Afanasiev, J. R. Hortensius, M. Matthiesen, S. Mañas-Valero, M. Šiškins, M. Lee, E. Lesne, H. S. van der Zant, P. G. Steeneken, B. A. Ivanov, E. Coronado, and A. D. Caviglia, Controlling the anisotropy of a van der Waals antiferromagnet with light, *Science Advances* **7**, 1 (2021).
- [25] S. Acharya, D. Pashov, A. N. Rudenko, M. Rösner, M. van Schilfgaarde, and M. I. Katsnelson, Real- and momentum-space description of the excitons in bulk and monolayer chromium tri-halides, *npj 2D Materials and Applications* **6**, 33 (2022).
- [26] M. Wu, Z. Li, and S. G. Louie, Optical and magneto-optical properties of ferromagnetic monolayer CrBr₃: A first-principles GW and GW plus Bethe-Salpeter equation study, *Physical Review Materials* **6**, 014008 (2022).
- [27] L. Zhu and L. Yang, Quasiparticle energies and excitonic effects of chromium trichloride: From two dimensions to bulk, *Physical Review B* **101**, 245401 (2020).
- [28] P. Abbamonte, T. Graber, J. P. Reed, S. Smadici, C.-L. Yeh, A. Shukla, J.-P. Rueff, and W. Ku, Dynamical reconstruction of the exciton in LiF with inelastic x-ray scattering, *Proceedings of the National Academy of Sciences* **105**, 12159 (2008).
- [29] T. Lettmann and M. Rohlfing, Finite-momentum excitons in rubrene single crystals, *Physical Review B* **104**, 115427 (2021).
- [30] G. Wang, A. Chernikov, M. M. Glazov, T. F. Heinz, X. Marie, T. Amand, and B. Urbaszek, Colloquium : Excitons in atomically thin transition metal dichalcogenides, *Reviews of Modern Physics* **90**, 021001 (2018).
- [31] W. He, Y. Shen, K. Wohlfeld, J. Sears, J. Li, J. Pelliari, M. Walicki, S. Johnston, E. Baldini, V. Bisogni, M. Mitrano, and M. P. M. Dean, Magnetically propagating Hund's exciton in van der Waals antiferromagnet NiPS₃, *Nature Communications* **15**, 3496 (2024).
- [32] C.-H. Chen and H.-F. Meng, Defect Auger exciton dissociation and impact ionization in conjugated polymers, *Physical Review B* **64**, 125202 (2001).
- [33] H. Wang, J. H. Strait, C. Zhang, W. Chan, C. Manolatos, S. Tiwari, and F. Rana, Fast exciton annihilation by capture of electrons or holes by defects via Auger scattering in monolayer metal dichalcogenides, *Physical Review B* **91**, 165411 (2015).
- [34] Y. Zhao, L. Lin, Q. Zhou, Y. Li, S. Yuan, Q. Chen, S. Dong, and J. Wang, Surface Vacancy-Induced Switchable Electric Polarization and Enhanced Ferromagnetism in Monolayer Metal Trihalides, *Nano Letters* **18**, 2943 (2018).
- [35] C. Wang, X. Zhou, Y. Pan, J. Qiao, X. Kong, C.-C. Kaun, and W. Ji, Layer and doping tunable ferromagnetic order in two-dimensional CrS₂ layers, *Physical Review B* **97**, 245409 (2018).
- [36] M. Pizzochero, Atomic-scale defects in the two-dimensional ferromagnet CrI₃ from first principles, *Journal of Physics D: Applied Physics* **53**, 244003 (2020).
- [37] Y. Guo, S. Yuan, B. Wang, L. Shi, and J. Wang, Half-metallicity and enhanced ferromagnetism in Li-adsorbed ultrathin chromium triiodide, *Journal of Materials Chemistry C* **6**, 5716 (2018).
- [38] Q. Yang, X. Hu, X. Shen, A. V. Krasheninnikov, Z. Chen, and L. Sun, Enhancing Ferromagnetism and Tuning Electronic Properties of CrI₃ Monolayers by Adsorption of Transition-Metal Atoms, *ACS Applied Materials and Interfaces* **13**, 21593 (2021).
- [39] M. Luo, Y. Li, K. Wang, and Y. Shen, Adsorption induced magnetic anisotropy in the two-dimensional magnet CrCl₃, *Solid State Communications* **321**, 114048 (2020).
- [40] R. V. Mikhaylovskiy, T. J. Huisman, V. A. Gavrichkov, S. I. Polukeev, S. G. Ovchinnikov, D. Afanasiev, R. V. Pisarev, T. Rasing, and A. V. Kimel, Resonant Pumping of d-d Crystal Field Electronic Transitions as a Mechanism of Ultrafast Optical Control of the Exchange Interactions in Iron Oxides, *Physical Review Letters* **125**, 157201 (2020).
- [41] A. Ron, S. Chaudhary, G. Zhang, H. Ning, E. Zoghlin, S. D. Wilson, R. D. Averitt, G. Refael, and D. Hsieh, Ultrafast Enhancement of Ferromagnetic Spin Exchange Induced by Ligand-to-Metal Charge Transfer, *Physical Review Letters* **125**, 197203 (2020).
- [42] A. V. Kimel, A. Kirilyuk, F. Hansteen, R. V. Pisarev, and T. Rasing, Nonthermal optical control of magnetism and ultrafast laser-induced spin dynamics in solids, *Journal of Physics: Condensed Matter* **19**, 043201 (2007).
- [43] N. Shimamoto, S.-i. Ohkoshi, O. Sato, and K. Hashimoto, Control of Charge-Transfer-Induced Spin Transition Temperature on Cobalt-Iron Prussian Blue Analogues, *Inorganic Chemistry* **41**, 678 (2002).
- [44] V. Pinchetti, Q. Di, M. Lorenzon, A. Camellini, M. Fasoli, M. Zavelani-Rossi, F. Meinardi, J. Zhang, S. A. Crooker, and S. Brovelli, Excitonic pathway to photoinduced magnetism in colloidal nanocrystals with nonmagnetic dopants, *Nature Nanotechnology* **13**, 145 (2018).
- [45] M. A. McGuire, G. Clark, S. KC, W. M. Chance, G. E. Jellison, V. R. Cooper, X. Xu, and B. C. Sales, Magnetic behavior and spin-lattice coupling in cleavable van der Waals layered CrCl₃ crystals, *Physical Review Materials* **1**, 014001 (2017).
- [46] X. Cai, T. Song, N. P. Wilson, G. Clark, M. He, X. Zhang, T. Taniguchi, K. Watanabe, W. Yao, D. Xiao, M. A. McGuire, D. H. Cobden, and X. Xu, Atomically Thin CrCl₃: An In-Plane Layered Antiferromagnetic Insulator, *Nano Letters* **19**, 3993 (2019).
- [47] Z. Wang, M. Gibertini, D. Dumcenco, T. Taniguchi, K. Watanabe, E. Giannini, and A. F. Morpurgo, Determining the phase diagram of atomically thin layered antiferromagnet CrCl₃, *Nature Nanotechnology* **14**, 1116 (2019).
- [48] D. R. Klein, D. MacNeill, Q. Song, D. T. Larson, S. Fang, M. Xu, R. A. Ribeiro, P. C. Canfield, E. Kaxiras, R. Comin, and P. Jarillo-Herrero, Enhancement of interlayer exchange in an ultrathin two-dimensional magnet, *Nature Physics* **15**, 1255 (2019).
- [49] H. H. Kim, B. Yang, S. Li, S. Jiang, C. Jin, Z. Tao, G. Nichols, F. Sfigakis, S. Zhong, C. Li, S. Tian, D. G. Cory, G.-X. Miao, J. Shan, K. F. Mak, H. Lei, K. Sun, L. Zhao, and A. W. Tsien, Evolution of interlayer and intralayer magnetism in three atomically thin chromium trihalides, *Proceedings of the National Academy of Sciences* **116**, 11131 (2019).
- [50] A. Bedoya-Pinto, J.-r. Ji, A. K. Pandeya, P. Gargiani, M. Valvidares, P. Sessi, J. M. Taylor, F. Radu, K. Chang,

- and S. S. P. Parkin, Intrinsic 2D-XY ferromagnetism in a van der Waals monolayer, *Science* **374**, 616 (2021).
- [51] L. Thiel, Z. Wang, M. A. Tschudin, D. Rohner, I. Gutiérrez-Lezama, N. Ubrig, M. Gibertini, E. Gianini, A. F. Morpurgo, and P. Maletinsky, Probing magnetism in 2D materials at the nanoscale with single-spin microscopy, *Science* **364**, 973 (2019).
- [52] Q.-C. Sun, T. Song, E. Anderson, A. Brunner, J. Förster, T. Shalomayeva, T. Taniguchi, K. Watanabe, J. Gräfe, R. Stöhr, X. Xu, and J. Wrachtrup, Magnetic domains and domain wall pinning in atomically thin CrBr₃ revealed by nanoscale imaging, *Nature Communications* **12**, 1989 (2021).
- [53] T. Song, Q.-C. Sun, E. Anderson, C. Wang, J. Qian, T. Taniguchi, K. Watanabe, M. A. McGuire, R. Stöhr, D. Xiao, T. Cao, J. Wrachtrup, and X. Xu, Direct visualization of magnetic domains and moiré magnetism in twisted 2D magnets, *Science* **374**, 1140 (2021).
- [54] X.-Y. Zhang, Y.-X. Wang, T. A. Tartaglia, T. Ding, M. J. Gray, K. S. Burch, F. Tafti, and B. B. Zhou, ac Susceptometry of 2D van der Waals Magnets Enabled by the Coherent Control of Quantum Sensors, *PRX Quantum* **2**, 030352 (2021).
- [55] Y.-X. Wang, X.-Y. Zhang, C. Li, X. Yao, R. Duan, T. K. M. Graham, Z. Liu, F. Tafti, D. Broido, Y. Ran, and B. B. Zhou, Visualization of bulk and edge photocurrent flow in anisotropic Weyl semimetals, *Nature Physics* **19**, 507 (2023).
- [56] F. Fabre, A. Finco, A. Purbawati, A. Hadj-Azzem, N. Rougemaille, J. Coraux, I. Philip, and V. Jacques, Characterization of room-temperature in-plane magnetization in thin flakes of CrTe₂ with a single-spin magnetometer, *Physical Review Materials* **5**, 034008 (2021).
- [57] B. B. Zhou, P. C. Jerger, K.-H. Lee, M. Fukami, F. Mujid, J. Park, and D. D. Awschalom, Spatiotemporal Mapping of a Photocurrent Vortex in Monolayer MoS₂ Using Diamond Quantum Sensors, *Physical Review X* **10**, 011003 (2020).
- [58] D. A. Wahab, M. Augustin, S. M. Valero, W. Kuang, S. Jenkins, E. Coronado, I. V. Grigorieva, I. J. Vera-Marun, E. Navarro-Moratalla, R. F. L. Evans, K. S. Novoselov, and E. J. G. Santos, Quantum Rescaling, Domain Metastability, and Hybrid Domain-Walls in 2D CrI₃ Magnets, *Advanced Materials* **33**, 2004138 (2021).
- [59] I. Pollini and G. Spinolo, Intrinsic Optical Properties of CrCl₃, *physica status solidi (b)* **41**, 691 (1970).
- [60] V. M. Bermudez and D. S. McClure, Spectroscopic studies of the two-dimensional magnetic insulators chromium trichloride and chromium tribromide-I, *Journal of Physics and Chemistry of Solids* **40**, 129 (1979).
- [61] N. S. Ginsberg and W. A. Tisdale, Spatially Resolved Photogenerated Exciton and Charge Transport in Emerging Semiconductors, *Annual Review of Physical Chemistry* **71**, 1 (2020).
- [62] A. McAllister, D. Bayerl, and E. Kioupakis, Radiative and Auger recombination processes in indium nitride, *Applied Physics Letters* **112**, 251108 (2018).
- [63] J. Holler, L. Bauriedl, T. Korn, A. Seitz, F. Özyigit, M. Eichinger, C. Schüller, K. Watanabe, T. Taniguchi, C. Strunk, and N. Paradiso, Air tightness of hBN encapsulation and its impact on Raman spectroscopy of van der Waals materials, *2D Materials* **7**, 015012 (2020).
- [64] S. R. Tauchert, M. Volkov, D. Ehberger, D. Kazenwadel, M. Evers, H. Lange, A. Donges, A. Book, W. Kreuzpaintner, U. Nowak, and P. Baum, Polarized phonons carry angular momentum in ultrafast demagnetization, *Nature* **602**, 73 (2022).
- [65] S. Jiang, L. Li, Z. Wang, K. F. Mak, and J. Shan, Controlling magnetism in 2D CrI₃ by electrostatic doping, *Nature Nanotechnology* **13**, 549 (2018).
- [66] E. W. Lemmon, I. H. Bell, M. L. Huber, and M. O. McLinden, *NIST Standard Reference Database 23: Reference Fluid Thermodynamic and Transport Properties-REFPROP, Version 10.0* (National Institute of Standards and Technology, Standard Reference Data Program, Gaithersburg, USA, 2018).
- [67] D. Mastroianni, L. Ottaviano, J. Wang, J. Yang, F. Gao, M. Ali, G. D'Olimpio, A. Politano, S. Palleschi, S. Kazim, R. Gunnella, A. Di Cicco, A. Sgarlata, J. Strychalska-Nowak, T. Klimczuk, R. J. Cava, L. Lozzi, and G. Profeta, Emerging oxidized and defective phases in low-dimensional CrCl₃, *Nanoscale Advances* **3**, 4756 (2021).
- [68] L. Liu, K. Zhai, A. Nie, W. Lv, B. Yang, C. Mu, J. Xiang, F. Wen, Z. Zhao, Z. Zeng, Y. Gong, Y. Tian, and Z. Liu, Accelerated Degradation of CrCl₃ Nanoflakes Induced by Metal Electrodes: Implications for Remediation in Nanodevice Fabrication, *ACS Applied Nano Materials* **2**, 1597 (2019).
- [69] V. Paolucci, D. Mastroianni, V. Ricci, H. Świątek, T. Klimczuk, L. Ottaviano, and C. Cantalini, Two-Dimensional CrCl₃-Layered Trihalide Nanoflake Sensor for the Detection of Humidity, NO₂, and H₂, *ACS Applied Nano Materials* **7**, 3679 (2024).
- [70] S. Kim, S. Yoon, H. Ahn, G. Jin, H. Kim, M.-H. Jo, C. Lee, J. Kim, and S. Ryu, Photoluminescence Path Bifurcations by Spin Flip in Two-Dimensional CrPS₄, *ACS Nano* **16**, 16385 (2022).
- [71] M. Birowska, P. E. Faria Junior, J. Fabian, and J. Kunstmann, Large exciton binding energies in MnPS₃ as a case study of a van der Waals layered magnet, *Physical Review B* **103**, L121108 (2021).
- [72] S. Fu, K. Kang, K. Shayan, A. Yoshimura, S. Dadras, X. Wang, L. Zhang, S. Chen, N. Liu, A. Jindal, X. Li, A. N. Pasupathy, A. N. Vamivak, V. Meunier, S. Strauf, and E.-H. Yang, Enabling room temperature ferromagnetism in monolayer MoS₂ via in situ iron-doping, *Nature Communications* **11**, 2034 (2020).
- [73] L.-A. T. Nguyen, K. P. Dhakal, Y. Lee, W. Choi, T. D. Nguyen, C. Hong, D. H. Luong, Y.-M. Kim, J. Kim, M. Lee, T. Choi, A. J. Heinrich, J.-H. Kim, D. Lee, D. L. Duong, and Y. H. Lee, Spin-Selective Hole-Exciton Coupling in a V-Doped WSe₂ Ferromagnetic Semiconductor at Room Temperature, *ACS Nano* **15**, 20267 (2021).
- [74] C. W. Zollitsch, S. Khan, V. T. T. Nam, I. A. Verzhbitskiy, D. Sagkovits, J. O'Sullivan, O. W. Kennedy, M. Strungaru, E. J. G. Santos, J. J. L. Morton, G. Eda, and H. Kurebayashi, Probing spin dynamics of ultra-thin van der Waals magnets via photon-magnon coupling, *Nature Communications* **14**, 2619 (2023).
- [75] Y. Kubo, C. Grezes, A. Dewes, T. Umeda, J. Isoya, H. Sumiya, N. Morishita, H. Abe, S. Onoda, T. Ohshima, V. Jacques, A. Dréau, J.-F. Roch, I. Diniz, A. Auffeves, D. Vion, D. Esteve, and P. Bertet, Hybrid Quantum Circuit with a Superconducting Qubit Coupled to a Spin Ensemble, *Physical Review Letters* **107**, 220501 (2011).

- [76] D. MacNeill, J. T. Hou, D. R. Klein, P. Zhang, P. Jarillo-Herrero, and L. Liu, Gigahertz Frequency Antiferromagnetic Resonance and Strong Magnon-Magnon Coupling in the Layered Crystal CrCl₃, *Physical Review Letters* **123**, 047204 (2019).
- [77] S. R. Singamaneni, L. M. Martinez, J. Niklas, O. G. Poluektov, R. Yadav, M. Pizzochero, O. V. Yazyev, and M. A. McGuire, Light induced electron spin resonance properties of van der Waals CrX₃ (X = Cl, I) crystals, *Applied Physics Letters* **117**, 082406 (2020).
- [78] S. Fava, G. De Vecchi, G. Jotzu, M. Buzzi, T. Gebert, Y. Liu, B. Keimer, and A. Cavalleri, Magnetic field expulsion in optically driven YBa₂Cu₃O_{6.48}, *Nature* **632**, 75 (2024).
- [79] A. Zalic, S. Simon, S. Remennik, A. Vakahi, G. D. Gu, and H. Steinberg, FeTe_{0.55}Se_{0.45} van der Waals tunneling devices, *Physical Review B* **100**, 064517 (2019).
- [80] G. Kresse and D. Joubert, From ultrasoft pseudopotentials to the projector augmented-wave method, *Physical Review B* **59**, 1758 (1999).
- [81] J. P. Perdew, K. Burke, and M. Ernzerhof, Generalized Gradient Approximation Made Simple, *Physical Review Letters* **77**, 3865 (1996).
- [82] S. Grimme, J. Antony, S. Ehrlich, and H. Krieg, A consistent and accurate ab initio parametrization of density functional dispersion correction (DFT-D) for the 94 elements H-Pu, *The Journal of Chemical Physics* **132**, 154104 (2010).
- [83] Y. Yekta, H. Hadipour, E. Şaşıoğlu, C. Friedrich, S. A. Jafari, S. Blügel, and I. Mertig, Strength of effective Coulomb interaction in two-dimensional transition-metal halides MX₂ and MX₃ (M = Ti, V, Cr, Mn, Fe, Co, Ni; X = Cl, Br, I), *Physical Review Materials* **5**, 034001 (2021).
- [84] S. L. Dudarev, G. A. Botton, S. Y. Savrasov, C. J. Humphreys, and A. P. Sutton, Electron-energy-loss spectra and the structural stability of nickel oxide: An LSDA+U study, *Physical Review B* **57**, 1505 (1998).

I. APPENDIX A: SAMPLE DETAILS

The experimental results have been verified on multiple CrCl₃ crystals grown by two different academic groups and by a commercial vendor (2D Semiconductors; Fig. 5). For Figs. 1-4, the CrCl₃ crystals were synthesized by vacuum sublimation of chromium (III) chloride powder (99.9%) in a single-zone tube furnace. The powder material with a total mass of 500 mg was sealed inside an evacuated silica tube, which was transferred into the furnace and heated to 650 °C at 5 °C/min, kept at that temperature for 72 hours, and cooled to room temperature. Large crystals of CrCl₃ with millimeter-size lateral dimensions and micron-size thickness was obtained. For Figs. 6 and 7, the CrCl₃ crystals was synthesized by vacuum sublimation of chromium (III) chloride powder (99.9%, Strem, USA) in a two zone tube furnace in a quartz ampoule. 25 g of CrCl₃ were placed in an ampoule (50x250 mm) and melt sealed under high vacuum of diffusion pump with liquid nitrogen cold trap at pressure under 1×10^{-3} Pa. The sealed ampoule was placed in two zone horizontal furnace. First the growth zone was

heated on 700 °C, while the source zone was kept at 500 °C. After two days the thermal gradient was reversed and source zone was kept at 700 °C while the growth zone temperature was slowly reduced from 680 to 600 °C over a period of one week and for additional one week was kept at 600 °C. Over 90% of the material was transported forming plate crystals with size up to 30 mm and thickness under 0.1 mm.

Two diamond substrates are used in this work, both containing 200 ± 133 nm of ¹²C isotopically-purified diamond (>99.995% ¹²C as per secondary ion mass spectrometry characterization). Pre-growth, these electronic grade bulk diamond substrates (Element Six) were fine-polished (Syntek) down to ≤ 0.3 nm root mean square (RMS) surface roughness. Thereafter, they underwent a cycling inductively coupled plasma-reactive ion etch (ICP-RIE) to remove the polish-induced damage (five cycles of Ar 25 sccm, Cl₂ 40 sccm, 10 mTorr, 400 W ICP, 200 W bias and O₂ 50 sccm, 10 mTorr, 700 W ICP, 100 W bias). The ICP-RIE process resulted in ≈ 2.5 μm removal while maintaining ≤ 0.3 nm RMS. This was followed by a multi-step annealing process at $< 2 \cdot 10^{-6}$ Torr (1.6 °C/min ramp, 12 h at 200 °C, 8 h at 400 °C, 8 h at 850 °C, and 2 h at 1200 °C). Overgrowth was performed in a custom-configured microwave plasma chemical vapor deposition system (SEKI DIAMOND SDS6350) at 11.5 W/mm², 0.2:400 sccm ¹²CH₄:H₂, and maintained at ≈ 850 °C and 25 Torr. Both the hydrogen and the methane were purified to better than 8 and 6 “nines”, respectively, with the chamber being pumped down to $< 5 \cdot 10^{-8}$ Torr base pressure before growth. Before the introduction of the methane precursor, the hydrogen plasma was allowed to run for 20 min as to etch away any residual surface carbonaceous contaminants.

To create a shallow layer of NV centers, one diamond sample was implanted with 40 keV ¹⁴N ions at 10^{12} ions/cm² and annealed at 1050 °C in forming gas (5% H₂, 95% Ar) for two hours, while the other was implanted with 45 keV ¹⁵N ions 10^{12} ions/cm² and annealed at 1050 °C for three hours. At $B_{ext} = 141.5$ mT, the average Ramsey T_2^* coherence time on the bare diamond is 3 μs and the average Hahn echo T_2 coherence time is 80 μs. This T_2^* is a factor of ten longer than similar ensemble samples in non-isotopically purified diamond.

CrCl₃ and hBN flakes are exfoliated onto separate polydimethylsiloxane (PDMS) stamps using blue tape (Ultron 1009R) inside an argon-filled glovebox with nominal residual concentrations of O₂ and H₂O <0.01 ppm. Air-sensitive atomically thin samples are known to still undergo chemical reactions inside a glovebox, despite impurity gas concentrations beneath the detection limit of standard analyzers [79]. A few-layer CrCl₃ flake is then identified by optical contrast (Supplementary Section II). The target CrCl₃ flake is transferred onto the diamond substrate and encapsulated by a suitable hBN flake using sequential PDMS viscoelastic transfer at room temperature. The diamond substrate is taken out of the glovebox, mounted onto a sample holder, and loaded into a

closed-cycle optical cryostat (Montana Instruments) for pump-out and cool-down in less than 30 minutes.

II. APPENDIX B: NV CENTER MEASUREMENTS

NV magnetic imaging is performed in a custom-built, dual-beam cryogenic (4 K) confocal microscope by pixel-to-pixel scanning of a diffraction-limited probe beam (FWHM = 400 nm). The linearly-polarized pump beam is slightly defocused and has a FWHM around 1 μm . The two beams are overlapped by analyzing the reflected camera image off the diamond surface. Full details of the optical and electronic setup are provided in Supplementary Section III. Due to the long T_2^* in our isotopically purified diamond samples, we can use pulsed ODMR sequences with a long 800 ns π -pulse resonant with the $|m_s = 0\rangle \rightarrow |m_s = -1\rangle$ spin transition. Pulsed ODMR resolves the nitrogen hyperfine splitting and enhances the dc field (B_{NV}) sensitivity, but requires more data points per pixel (e.g., 25 frequency points to sample the triply-split ^{14}N resonance lineshape). For Hahn (Φ) imaging, we acquire four data points per pixel corresponding to four different phases for the final $\pi/2$ projection pulse (30 ns width): $X_{\pm\pi/2}$ and $Y_{\pm\pi/2}$, where the denoted X - and Y -axis Bloch sphere rotations are realized by in-phase (I) and quadrature (Q) modulation of the microwave drive. The X_P and Y_P projections are then determined differentially by $X_P = C(X_{-\pi/2}) - C(X_{+\pi/2})$ and $Y_P = C(Y_{-\pi/2}) - C(Y_{+\pi/2})$, where C denotes the integrated photon counts, and then normalized to the range ± 1 by the Rabi contrast.

III. APPENDIX C: DENSITY FUNCTIONAL THEORY CALCULATIONS

Spin-polarized DFT calculations are performed using the Vienna *Ab initio* Simulation Package (VASP) within the projector augmented wave method [80]. The electron exchange-correlation is described using the generalized gradient approximation as parameterized by Perdew-Burke-Ernzerhof [81]. The van der Waals interaction is

accounted for using the DFT+D3 approach [82]. The correlation effect is modeled by applying $U_{\text{eff}} = 3.5$ eV on the Cr $3d$ electrons [83] using the DFT+U approach developed by Dudarev *et al.* [84]. The kinetic energy cut-off is set to 400 eV. The first Brillouin zone is sampled by a two-dimensional Γ -centered k -point mesh with ~ 0.06 \AA intervals; for example, an $18 \times 18 \times 1$ mesh is used for a monolayer CrCl_3 primitive cell. Electronic energy convergence is achieved with a precision of 10^{-7} eV. Lattice and ionic relaxation processes are carried out until the Hellmann-Feynman forces exerted on each ion are reduced below 1 meV/ \AA .

IV. ACKNOWLEDGMENTS

The authors thank B. Flebus for valuable discussions. B.B.Z. acknowledges the National Science Foundation (NSF) CAREER award No. DMR-2047214 and NSF award No. ECCS-2041779. This material is based on work supported by the Air Force Office of Scientific Research under award no. FA2386-21-1-4095. B.Y. acknowledges the financial support by the European Research Council (ERC Consolidator Grant “NonlinearTopo”, No. 815869) and the ISF - Personal Research Grant (No. 2932/21). The diamond synthesis work was primarily supported by the U.S. Department of Energy, Office of Basic Energy Sciences, Materials Science and Engineering Division (N.D., J.A., D.D.A., F.J.H.). F.T. acknowledges support from the U.S. Department of Energy, Office of Basic Energy Sciences, Division of Physical Behavior of Materials under Award No. DE-SC0023124. Z.S. was supported by ERC-CZ program (project LL2101) from Ministry of Education Youth and Sports (MEYS) and used large infrastructure from project reg. No. CZ.02.1.01/0.0/0.0/15_003/0000444 financed by the EFRR. K.W. and T.T. acknowledge support from the JSPS KAKENHI (Grant Numbers 21H05233 and 23H02052) and World Premier International Research Center Initiative (WPI), MEXT, Japan. M.J. acknowledges support from IITP grant funded by the Korean government (MSIT) (2021-0-01511). This work was performed, in part, at the Integrated Sciences Cleanroom and Nanofabrication Facility at Boston College.